



# Ice motion across incised fjord landscapes

Sjur Barndon<sup>1, a</sup>, Robert Law<sup>1, 2</sup>, Andreas Born<sup>1, 2</sup>, Thomas Chudley<sup>3</sup>, and Stefanie Brechtelsbauer<sup>4</sup>

<sup>1</sup>University of Bergen, Department of Earth Science, Norway

<sup>2</sup>Bjerknes Centre for Climate Research, Norway

<sup>3</sup>Durham University, Department of Geography, UK

<sup>4</sup>Stockholm University, Department of Meteorology, Sweden

<sup>a</sup>Now at University of Bergen, Department of Biological Sciences, Norway

**Correspondence:** Sjur Barndon (sjurbarndon@proton.me)

**Abstract.** The thermodynamic behaviour of ice-sheet motion over rough landscapes is poorly understood, with most ice-sheet models prescribing a bed smoother than reality, which will not fully capture topographic features. Subglacial fjords striking obliquely to the palaeo flow direction are an extreme case, but are ubiquitous beneath the western margin of the palaeo Scandinavian Ice Sheet, and likely provide a useful proxy for areas of the present-day Greenland Ice Sheet. Here, we consider Veafjorden as a characteristic western Norwegian fjord where striations clearly evidence palaeo perpendicular ice flow, and perform 3D thermodynamically-coupled ice-motion simulations across a range of orientations. For perpendicular flow, surface velocity above the fjord is reduced substantially while a thick layer of temperate ice occupies the fjord. Moffatt eddies, or spiralling flows, occur in the fjord hollow with reverse-direction slip at the fjord base. When compared to smoothed topography, perpendicular flow over *real* topography requires  $\sim 41\text{--}89\%$  greater area-averaged driving stress, dependent on the overlying ice thickness, while a switch from fjord-parallel to fjord-perpendicular flow for real topography requires a  $\sim 28\text{--}45\%$  area-averaged driving-stress increase. These results may explain surface velocity variations at many locations towards the margins of the Greenland Ice Sheet, and imply that the role of anisotropic roughness in resisting ice-sheet motion may be significantly underappreciated. Last, we note that deep fjords provide a clear physically-based example for why bounded basal traction relationships (i.e. regularised-Coulomb) may not hold at the macro scale in rough settings.

## 1 Introduction

Basal topography exerts a critical control on ice-sheet motion at all scales considered (Kyrke-Smith et al., 2018; Helanow et al., 2021; Castleman et al., 2022; Frank et al., 2022; Wernecke et al., 2022; Law et al., 2023), but its influence at the intermediate scale — above the  $\sim 0.5\text{--}25$  m scale typically used to determine sliding parametrisations yet below the  $\sim 400\text{--}4,000$  m scale of resolution or basal topography fidelity of most ice sheet models — is particularly poorly constrained. Notably, the ice-motion influence of incised fjord landscapes remains almost entirely unexplored. This landscape characterises the terrestrial western margin of the palaeo Scandinavian Ice Sheet and provides a reasonable proxy for marginal areas of the Greenland Ice Sheet (GrIS) which share geological and topographic similarities (e.g. Gee et al., 2008; Christ et al., 2023; Paxman et al., 2024), as well as regions of the Antarctic Ice Sheet (AIS) such as the Aurora Subglacial Basin (Young et al., 2011). In the fjords of

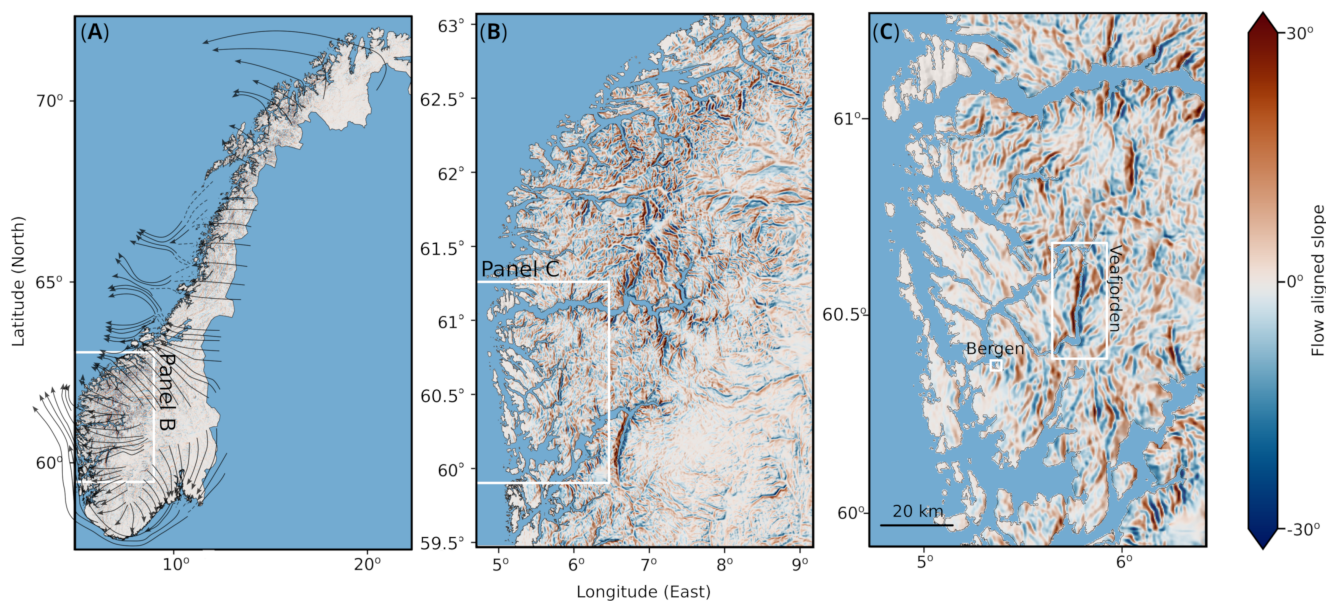


**Figure 1.** Slope calculated using the flow direction output of Jungdal-Olesen et al. (2024) for 32 kyr ago with Copernicus GLO-30 DEM data (Copernicus DEM, 2024). Positive values indicate an increase in elevation along the flow direction. Note that the maximum resolution of 60 m in panel C means that some small features (i.e. cliffs) may not be accurately resolved. Flow arrows in panel A adapted from Ottesen et al. (2005).

western Norway, striations (Kleman et al., 1997; Mangerud et al., 2019) and consideration of palaeo flow directions (Jungdal-  
 25 Olesen et al., 2024) evidence widespread perpendicular ice flow over deep subglacial fjords, as well as in obtuse and parallel  
 orientations (Fig. 1) with unclear implications for ice motion.

Ice motion across an idealised subglacial valley has been modelled in 2D and 3D in a relatively straightforward manner  
 (Gudmundsson, 1997; Meyer and Creyts, 2017), but not previously using actual topographic data and with the inclusion of  
 temperate ice rheology, implementation of a rate-dependent resistance for slip at the ice-bed boundary, or ‘fast’ ( $\geq 100 \text{ m a}^{-1}$ )  
 30 ice-surface velocity. Here, we incorporate these additional processes and consider fast ice motion for a section of the palaeo  
 Scandinavian Ice Sheet. We focus on Veafjorden close to the city of Bergen, Norway (Fig. 2) as a characteristic example with  
 a relief of  $\sim 1,300 \text{ m}$ , and a narrow  $\sim 2 \text{ km}$  width. Striation markings on both sides of Veafjorden confirm near-perpendicular  
 flow across the fjord around 15 kyr ago (Mangerud et al., 2019). The fjords were likely incised into pre-existing river valleys  
 and geological weaknesses through erosion as the Scandinavian Ice Sheet grew and shrank, but not at its fullest extent (Harbor  
 35 et al., 1988; Harbor, 1992; Briner et al., 2008; Bernard et al., 2021; Paxman, 2023; Reilly, 2023; Jungdal-Olesen et al., 2024),  
 however the general pattern of fjord formation in western Norway has not been comprehensively investigated to our knowledge.  
 In order to assess the difference in controls on ice motion between this *real* topography, and the smoother bed products used

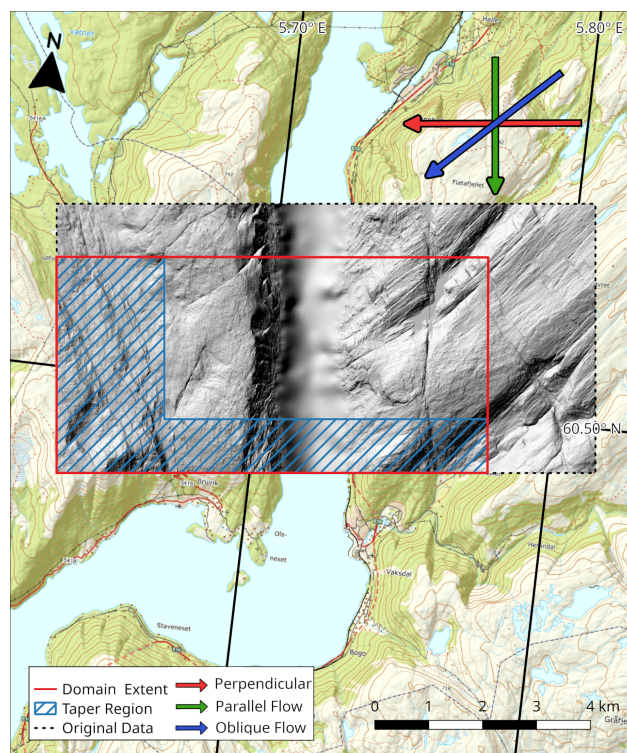


**Figure 2.** DEM of Veafjorden. The blue hatched area show the tapering region used in all simulations. The red, blue and green arrows displays the simulated flow directions. Perpendicular flow (red arrow) have been dated to 15 kyr BP and parallel flow (green arrow) at 11.5 kyr BP (Mangerud et al., 2019). Elevation data from the Norwegian Mapping Authority (Kartverket, 2024b, a).

to model the GrIS and AIS (BedMachine and BedMap), we additionally create a smoothed representation of Veafjorden. This substitute provides an opportunity to examine the impact of the generally low fidelity elevation models presently in use.

40 Our simulations can therefore reveal the influence of realistic anisotropic basal conditions. Over a single glacial cycle, the orientation of ice motion will vary (Jungdal-Olesen et al., 2024), while the landscape will remain effectively immutable. The simulations presented here, and consideration of how these extend to the broader palaeo Scandinavian Ice Sheet, indicate that over rough topography complex basal motion patterns should be expected as the norm rather than the exception. Finally, while our simulations reveal ice thermodynamics over fjords in great detail, considerations of simple aspects of fjord geometry  
45 and viscous ice deformation within them further point towards the influence such landscapes should exert on intermediate, or macro, scale sliding relationships.

## 2 Methods

We model 3D ice motion over an 8 km by 4 km rectangular domain covering Veafjorden (Fig. 2). The Digital Elevation Model (DEM) was constructed at a resolution of 20 m with data from Kartverket (The Norwegian Mapping Authority), combining



50 terrestrial data at 1 m (Kartverket, 2024b), with the fjord bathymetry interpolated from a 50 m resolution data set (Kartverket,  
2024a). To conform to the models periodic boundary conditions the inflow and outflow boundaries must match. We achieved  
this using a tapering algorithm following Helanow et al. (2021), with one third of the down-flow length and width of the domain  
added as a tapering region that then matches the topography at the inflow boundary (Fig. 2). We applied a Gaussian filter with  
a standard deviation of 1.5 to the DEM to smooth out artifacts and sharp edges which can present model stability issues (Law  
55 et al., 2023).

The domain was discretised in Elmer/Ice Version 9.0 (Gagliardini et al., 2013) with a triangular mesh with a representative  
element side length of 25 m and 20–30 vertical layers with resolution increasing towards the base (with a representative side  
length of 100 m and 15 vertical layers for the smoothed topography simulation with 500 m plateau ice thickness). First, the free  
surface is allowed to vary and the inflow and outflow and two lateral boundaries are matched periodically for velocity, stress,  
60 and free-surface position. Second, the free surface and the inflow velocity fields are fixed and the enthalpy field is allowed  
to evolve without a periodic boundary condition requirement. Outflow/side boundaries are set at lithostatic pressure/zero flux  
depending on simulation orientation (Fig. A1).

The central equations and boundary conditions are as follows, with additional model background in Law et al. (2023). Table  
A1 lists all parameter values. We solve the standard Stokes equations for ice flow

$$65 \quad \nabla \cdot \mathbf{u} = 0 \quad (\text{conservation of mass}) \quad (1)$$

$$\nabla \cdot \boldsymbol{\tau} - \nabla p = -\rho \mathbf{g} \quad (\text{conservation of momentum}) \quad (2)$$

where  $\mathbf{u}$  ( $\text{m a}^{-1}$ ) is the velocity vector,  $\boldsymbol{\tau}$  (MPa) is the deviatoric stress tensor,  $p$  (MPa) is ice pressure,  $\rho$  ( $\text{kg m}^{-3}$ ) is the ice  
density and  $\mathbf{g}$  is the gravity vector described as

$$\mathbf{g} = [g \sin(\theta), 0, -g \cos(\theta)] \quad (3)$$

70 where  $g = 9.81 \text{ m s}^{-2}$  and  $\theta$  is the domain slope. Adjusting the orientation of  $\mathbf{g}$  removes the requirement for vertical displace-  
ment of periodic inflow-outflow boundaries.

Stress is related to strain using the Nye-Glen isotropic flow law (Nye, 1953; Glen, 1955; Cuffey and Paterson, 2010):

$$\dot{\boldsymbol{\epsilon}} = A \tau_e^{n-1} \boldsymbol{\tau} \quad (4)$$

where  $\dot{\boldsymbol{\epsilon}}$  is the strain rate tensor,  $\tau_e^2 = \frac{1}{2} \text{tr}(\boldsymbol{\tau}^2)$  (MPa) is the effective stress in the ice,  $n$  is the flow exponent set to 3, and  $A$   
75 ( $\text{MPa}^{-3} \text{a}^{-1}$ ) is the creep parameter.  $A$  is set using the homologous temperature,  $T_h$  (K), below the pressure melting point,  $T_m$ ,  
or water fraction,  $\omega$ , when above the pressure melting point:

$$A = \begin{cases} A_1 \exp\left(\frac{Q_1}{RT_h}\right), & T_h \leq T_{\text{lim}} \\ A_2 \exp\left(\frac{Q_2}{RT_h}\right), & T_{\text{lim}} < T_h < T_m \\ (W_1 + W_2 \omega \times 100) W_3, & T_h \geq T_m \text{ and } \omega < \omega_{\text{lim}} \\ A_{\text{max}}, & \omega \geq \omega_{\text{lim}} \end{cases} \quad (5)$$



where  $T_m(p) = T_{tr} - \gamma(p - p_{tr})$  and  $\gamma$  ( $\text{K MPa}^{-1}$ ) is the Clausius-Clapeyron constant, and  $T_{tr}$  and  $p_{tr}$  are the temperature and pressure triple points for water, respectively.  $A_1$  and  $A_2$  ( $\text{MPa a}^{-1}$ ) are rate factors,  $Q_1$  and  $Q_2$  ( $\text{J mol}^{-1}$ ) are activation energies for  $T \leq T_{lim}$  and  $T_{lim} < T < T_m$ , respectively, where  $T_{lim}$  is the limit temperature.  $R$  ( $\text{J mol}^{-1}$ ) is the gas constant,  $W_1$ ,  $W_2$  and  $W_3$  ( $\text{MPa a}^{-1}$ ) are water viscosity factors (constant for all simulations) with default values from Haseloff et al. (2019) adapted from Duval (1977). The liquid water fraction limit,  $\omega_{lim}$  is set to 2.5% following experiments of Adams et al. (2021). If  $\omega_{lim}$  is exceeded then  $A$  is limited to a maximum value  $A_{max}$ . Very recent studies propose  $n = 1$ , or different relationships for  $A$  for temperate ice (Schohn et al., 2025; Roldán-Blasco et al., 2025), but we leave exploration of these parameters for a future study. Values for these and subsequent parameters are provided in Table A1.

Within the Elmer/Ice EnthalpySolver (Gilbert et al., 2014), specific enthalpy,  $H$  ( $\text{J kg}^{-1}$ ), is used as the state variable and is related to  $T$  and  $\omega$  as

$$H(T, \omega) = \begin{cases} \frac{1}{2}C_a (T^2 - T_{ref}^2) & H < H_m(p) \\ + C_b (T - T_{ref}), & \\ \omega L + H_m, & H \geq H_m(p) \end{cases} \quad (6)$$

where  $C_a$  ( $\text{J kg}^{-1} \text{K}^{-2}$ ) and  $C_b$  ( $\text{J kg}^{-1} \text{K}^{-1}$ ) are enthalpy heat capacity constants,  $L$  ( $\text{J kg}^{-1}$ ), is the latent heat capacity of ice,  $H_m(p) = \frac{1}{2}C_a (T_m(p)^2 - T_{ref}^2) + C_b (T_m(p) - T_{ref})$  is the specific enthalpy at the pressure melting point, and  $T_{ref}$  is the reference temperature.

Change in the position of the free surface,  $s$ , is calculated as

$$\frac{\delta s}{\delta t} + u_x \frac{\delta s}{\delta x} + u_y \frac{\delta s}{\delta y} = u_z \quad (7)$$

in the Elmer/Ice FreeSurfaceSolver where  $u_x$ ,  $u_y$ , and  $u_z$  are components of  $\mathbf{u}$ .

At each time step, the enthalpy field is evolved until a steady-state is reached and is calculated as

$$\rho \left( \frac{\partial H}{\partial t} + \mathbf{u} \cdot \nabla H \right) = \nabla \cdot (\kappa \nabla H) + \text{tr}(\boldsymbol{\tau} \dot{\boldsymbol{\epsilon}}) \quad (8)$$

(conservation of energy)

where  $\text{tr}(\boldsymbol{\tau} \dot{\boldsymbol{\epsilon}})$  is the strain heating term and  $\kappa$  ( $\text{kg m}^{-1} \text{s}^{-1}$ ) is the enthalpy diffusivity defined as

$$\kappa = \begin{cases} \kappa_c, & H < H_m(p) \\ \kappa_t, & H \geq H_m(p) \end{cases} \quad (9)$$

where  $\kappa_c$  and  $\kappa_t$  are enthalpy diffusivities for cold and temperate ice respectively, meaning that water movement within the temperate ice is assumed to be a diffusive process.



The lower boundary velocity is set to zero normal to the surface (impenetrability condition at base):

$$\mathbf{u} \cdot \mathbf{n} = 0 \text{ where } z = 0 \quad (10)$$

where  $\mathbf{u}$  is the velocity vector and  $\mathbf{n}$  is the normal vector to the bedrock. Basal traction  $\tau_b$  is calculated following Helanow et al. (2021) as:

$$\tau_b = CN_e \left( \frac{u_b^{-n+1}}{u_b + A_s C^n N_e^n} \right)^{\frac{1}{n}} u_b \quad (11)$$

where  $C$  (dimensionless) is a parameter dependant on basal morphology (Helanow et al., 2021).  $N_e = p_i - p_w$  (MPa) is the effective pressure at the bed where  $p_i$  (MPa) is the ice overburden pressure and  $p_w$  (MPa) is the subglacial water pressure.  $u_b$  ( $\text{m a}^{-1}$ ) is the basal velocity tangential to the ice-bed interface. The flow exponent  $n$  is the same as for the strain rate equal to

110 3.  $A_s$  ( $\text{m a}^{-1} \text{MPa}^{-3}$ ) is the average sliding coefficient based on six values from Helanow et al. (2021).

## 2.1 Simulation ensemble

We simulate variations in flow direction, target surface velocity, and the thickness of ice over the plateau (measured from the highest point within the domain), as well as a smoothed control run with ice motion perpendicular to the fjord. We selected two ice thicknesses, 500 m and 1,000 m, both within the modelled ice thickness of previous studies (Svendsen and Mangerud, 1987; Mangerud et al., 2019) and which provide a reasonable range for exploring the role of ice thickness on flow patterns before fjord geometry begins to influence flow direction (Reilly, 2023). Two target surface velocities were selected,  $450 \text{ m a}^{-1}$  and  $850 \text{ m a}^{-1}$ , based on the surface velocity at bore-hole locations with matching ice thickness in Greenland (Løkkegaard et al., 2023). Three flow directions are simulated, perpendicular ( $90^\circ$ ), oblique ( $45^\circ$ ) and parallel ( $0^\circ$ ). An overview of all simulations can be found in Table 1 and Fig. 3. The smoothed topography was created by applying a Gaussian filter with a standard deviation of 50 to the original DEM.

115  
120

To reach a target surface velocity, a low fidelity (resolution of 100 m with 10 extruded mesh levels) simulation was used with an ad-hoc approach to tests using increments of  $0.05^\circ$  for  $\theta$ . The value that produced the closest-to-target average surface velocity (values displayed in Table 1) was then used in subsequent full-resolution simulations. We convert the resulting slope to driving stress for comparison. Driving stress,  $\tau_d$ , is calculated from ice thickness,  $H$ , and the slope used to adjust the gravity vector orientation,  $\theta$ , as

125

$$\tau_d = \rho g H \sin(\theta). \quad (12)$$

Note that the  $H$  used in  $\tau_d$  is the average ice thickness of the domain giving 1398.6 m and 898.6 m for 1,000 m and 500 m above the plateau respectively. The smoothed topography DEM yields the averages of 1222.6 m and 722.6 m for plateau ice thickness 1,000 m and 500 m respectively.



### 130 3 Results

Our results demonstrate the strong control that subglacial fjords, and their orientation with respect to ice motion direction, exert on ice-sheet motion (Fig. 3). For flow-perpendicular simulations, Moffat eddies and basal flow reversal occurs for both 500 m and 1,000 m ice thickness above plateau, but only with real (i.e. not smoothed) topography. Deep perpendicularly-oriented valleys beneath an ice sheet also significantly impede overlying ice motion — comparing one smoothed simulation (8Sm10, see Table 1) to its real topography counterpart (8Pe10) yields an increase in slope of 25.8%, equivalent to a change in area-averaged driving stress from 295.2 – 424.8 kPa (44%). Alternative fjord orientations also significantly influence both motion patterns and temperate ice distribution patterns. Here, we cover the following aspects: (3.1) perpendicular flow and the associated formation of Moffat eddies, (3.2) parallel flow, and (3.3) separation of flow in oblique-orientation simulations. Last, (3.4) we compare smoothed-topography control simulations to their real counterparts.

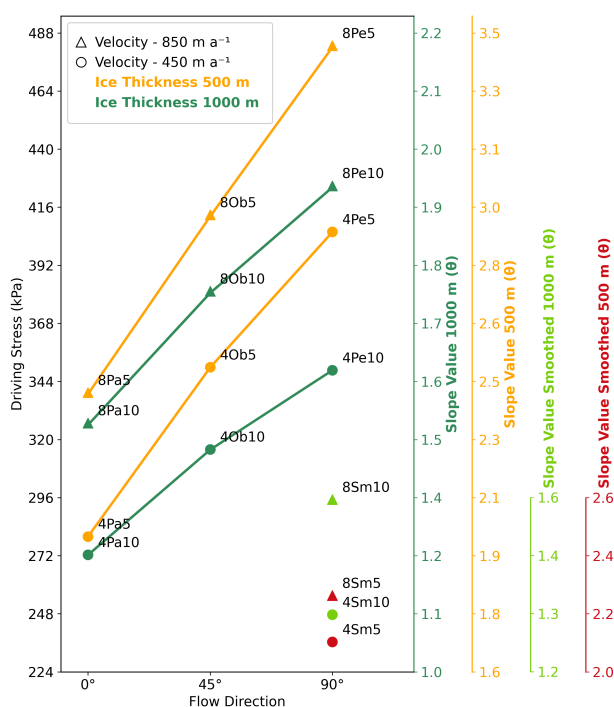


**Figure 3.** Resulting driving stress values for each selected flow direction, ice thickness and velocity target. Simulations with velocity target of  $450 \text{ m a}^{-1}$  are marked with circles, while  $850 \text{ m a}^{-1}$  are triangles. Simulations in green have a plateau ice thickness of 1,000 m while orange indicates a 500 m thickness. Average ice thickness was used in the driving stress calculation. Smoothed topography simulations have separate ice thickness values (See 2.1). The label for each marker are individual run IDs corresponding to Table 1.



**Table 1.** An overview of simulated scenarios and results. Flow direction is relative to the orientation of Veafjorden. Ice thicknesses are defined from the highest point of the domain. Simulation IDs reflect the variables used, ordered by velocity target, flow direction, and ice thickness. For example the base simulation of Veafjorden with target surface velocity of 850 perpendicular flow, and plateau ice thickness of 1,000 m is 8Pe10. The corresponding simulation with 500 m ice thickness is 8Pe5.

Target Surface Velocity ( $\text{m a}^{-1}$ )	Flow Direction	Plateau Ice Thickness (m)	Slope $\theta$ ( $^\circ$ )	Driving Stress (kPa)	ID	Surface Velocity Mean ( $\text{m a}^{-1}$ )	Target Velocity Deviation ( $\text{m a}^{-1}$ )	
450 m/a	Perpendicular	1,000	1.60	348.61	4Pe10	479.8	29.8	
		500	2.90	405.8	4Pe5	531.4	81.4	
	Parallel	1,000	1.25	272.4	4Pa10	482.4	32.4	
		500	2.00	279.9	4Pa5	418.1	-31.9	
	Oblique	1,000	1.45	315.9	4Ob10	464.1	14.1	
		500	2.50	349.9	4Ob5	463.2	13.2	
	Perpendicular (Smoothed Control)	1,000	1.30	247.6	4Sm10	468.3	18.3	
		500	2.10	236.4	4Sm5	478.7	28.9	
	850 m/a	Perpendicular	1,000	1.95	424.8	8Pe10	844.3	-5.7
			500	3.45	482.7	8Pe5	871.4	21.4
Parallel		1,000	1.50	326.8	8Pa10	860.3	10.3	
		500	2.425	339.4	8Pa5	872.0	22.0	
Oblique		1,000	1.75	381.3	8Ob10	829.2	-20.8	
		500	2.95	412.8	8Ob5	837.4	-12.6	
Perpendicular (Smoothed Control)		1,000	1.55	295.2	8Sm10	868.4	18.4	
		500	2.27	255.5	8Sm5	815.3	-34.7	

### 140 3.1 Perpendicular flow direction

Across all target velocities and plateau ice thickness combinations for perpendicular flow over real topography Moffatt eddies (Moffatt, 1964a, b) form at the base of the fjord, accompanied by spiralling lateral ice motion along the lowermost fjord depression. Ice velocity is also greatly affected by the topography. For simulations with target surface velocity of 850  $\text{m a}^{-1}$  (8Pe10), the surface directly above the fjord velocity is reduced by  $\sim 120 \text{ m a}^{-1}$  (Fig. 7d), while absolute velocity within the  
145 fjord the plateau elevation drops below  $500 \text{ m a}^{-1}$  (Fig. 4c). This velocity difference creates a distinct shear margin that spans the fjord from crest to crest across the width of the entire domain (Fig. 4). The eddies that form under this sheer margin are up to 570 m in diameter. In the case of simulation 8Pe10 with target velocity of 850  $\text{m a}^{-1}$  and ice thickness of 1,000 m a secondary set of eddies is also simulated (Fig. 5b).

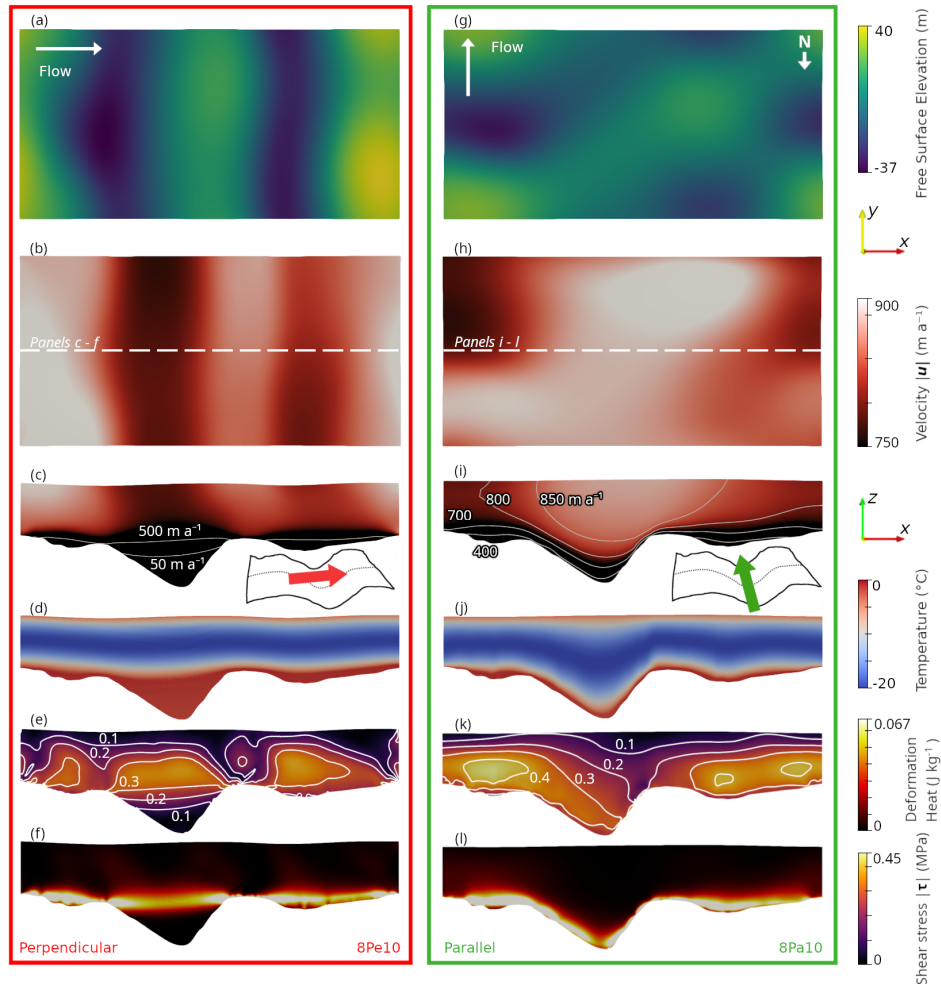


**Figure 4.** Free surface elevation and velocity of perpendicular 8Pe10 (a–f) and parallel 8Pa10 (g–l) simulations. Panel (a, g) show the free surface elevation, (b, h) show the corresponding surface velocity ( $\text{m a}^{-1}$ ). Panel (c, g) is the velocity field of the cross section from the centre of the domain. Panel (d, h) show temperature ( $^{\circ}\text{C}$ ) at the same cross section. Panel (e, k) show deformation heat ( $\text{J kg}^{-1}$ ) and panel (f, l) is the shear stress (MPa).

Flow from the tributary valley on the upslope plateau, feeds ice flow into the Moffatt eddies. Upon entering the fjord from the  
 150 tributary, the Moffatt eddy splits laterally, resulting in two independent eddies transporting ice in opposite directions along the  
 fjord. In the free surface runs where periodic lateral boundaries are present (and temperate ice is not) ice is exchanged laterally  
 through the boundary in both positive and negative y orientations, as well as returning back to the main overriding flow. When  
 no-flux boundaries replace lateral periodic boundaries in the thermomechanically coupled runs more ice is directed back into  
 the overriding flow towards the domain edges. The maximum y-oriented velocity within the fjord is  $\sim 27 \text{ m a}^{-1}$  (8Pe10).

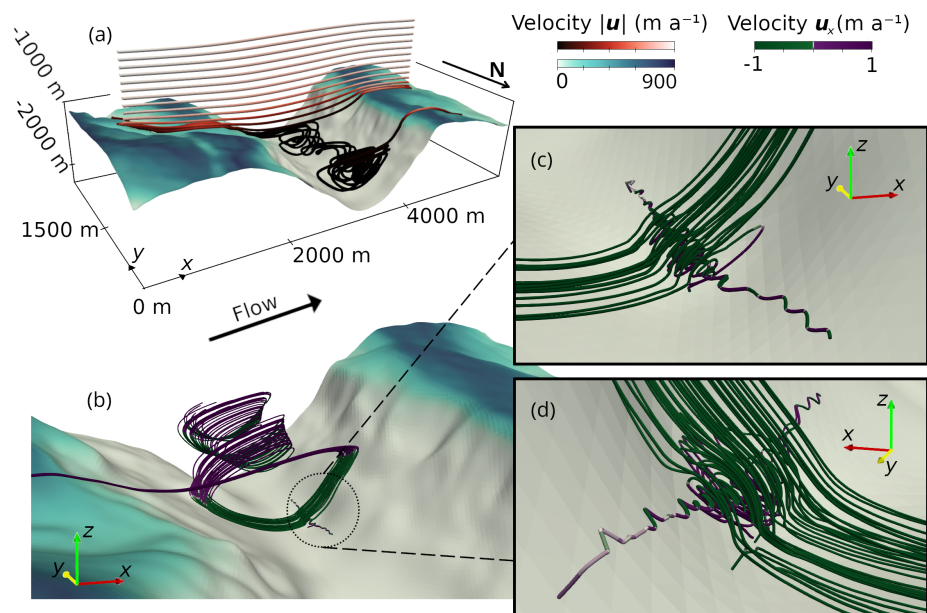


**Figure 5.** Streamline velocity for perpendicular, 1,000 m plateau ice thickness run 8Pe10. Streamlines show that ice from the plateau enters an eddy in the valley, moves laterally, and reappears far to the north on the other side (a). Streamlines of (a) coloured by velocity magnitude. Secondary Moffatt eddy forms in a small depression in the valley side (b). Streamlines coloured for x direction velocity (b–d), constrained from  $-1$  to  $1 \text{ m a}^{-1}$  showing reversal of flow. Target surface velocity  $850 \text{ m a}^{-1}$ .

155 Just below the margin between the Moffatt eddies in the fjord, and the overflowing ice above, there is a reduction in liquid water content. Partial refreezing of meltwater occurs as the eddies rise on the up-slope fjord side (Fig. 6a.ii). From a Lagrangian viewpoint, the rise increases the pressure melting point and lowers the specific enthalpy at the pressure melting point ( $H_m(p)$ ) meaning the melt fraction decreases so that the overall specific enthalpy does not change. This temperate ice water content margin is present along the entire valley, following the meeting point between eddy movement and overlaying ice (Fig. 6a.i).

160 High stresses and deformation heating between the fjord crests (Fig. 4e,f) results in the formation of a deep temperate layer found in perpendicular simulations (Fig. 6a).

### 3.2 Parallel flow direction

We use the domain slope and hence domain-averaged driving stress as the main lever to adjust the area-averaged surface velocity. Considering a change in flow direction from parallel to perpendicular over the real topography with an ice thickness above the plateau of 1,000 m, the slope must be altered by  $0.45^\circ$ , corresponding to an increase in averaged driving stress from 326.8 to 424.8 kPa (8Pa10 and 8Pe10 respectively). This substantial difference in driving stress between parallel and perpendicular flow indicates the anisotropic nature of a landscapes resistance to flow dependent on its orientation (Fig. 4). The change in slope required to match surface velocity for parallel and perpendicular topography is similar to the difference between actual bed

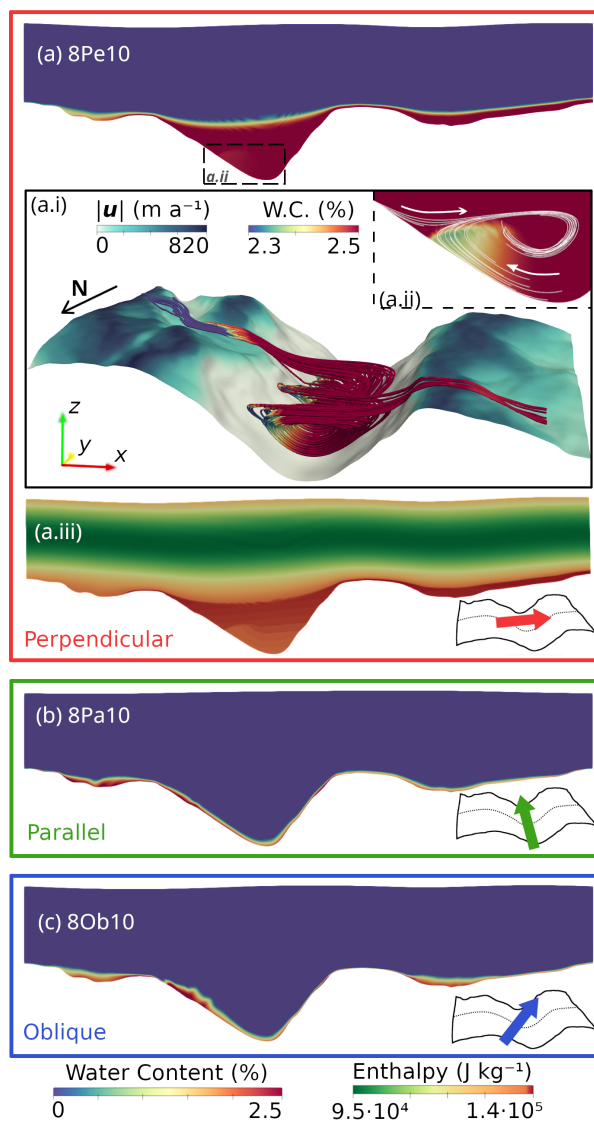


**Figure 6.** Temperate ice water content comparison of perpendicular (a), parallel (b), and oblique (c) flow direction. Cross sections taken from the centre of the domain. Panel (a.iii) show the enthalpy field of the same cross-section as (a). A change in enthalpy can be spotted along the same margin where the temperate ice water content is reduced in the fjord.

topography and the smoothed topography ( $0.40^\circ$  for simulations 8Pe10, 8Sm10) when both are in the perpendicular orientation  
 170 (Table 2). The influence of a parallel oriented-fjord on surface elevation and velocity is fairly small, with a much more uniform  
 decrease in velocity with depth when compared to the flow-perpendicular simulations. The temperate ice layer thickness for  
 parallel runs is uniformly much lower than for perpendicular runs, with no large volume of temperate ice occupying the fjord  
 hollow (Fig. 6b).



**Table 2.** Mean slope and driving stress changes for varying simulation comparisons. Taking the average of the differences from all simulation flow directions, ice thicknesses and velocity targets. Smoothed control simulations are excluded from the velocity target comparison and the flow direction comparison.

Comparison		Mean Slope Difference(°)	Mean Driving Stress Difference (kPa)	Mean Driving Stress Change (%)
Parallel flow (IDs: *Pa**)	→ Perpendicular flow (IDs: *Pe**)	0.68	110.9	36.3
Perpendicular (Smoothed) (IDs: *Sm**)	→ Perpendicular flow (IDs: *Pe**)	0.67	156.8	61.3
450 m a <sup>-1</sup> (IDs: 4****)	→ 850 m a <sup>-1</sup> (IDs: 8****)	0.39	65.9	18.5

### 3.3 Oblique flow direction

175 In the simulations with oblique flow the flow direction is vertically stratified. At the base of the fjord, the flow aligns with the fjord orientation, while surface flow aligns with the surface slope (Fig. A3). However, surface flow does not directly follow the domain slope (Eq. 3), but deviates from it due to the topographic steering at depth. The simulation with 1,000 m plateau ice thickness and target velocity of 450 m a<sup>-1</sup> (4Ob10) has a surface flow direction change of 17.1° while the corresponding simulation of 500 m plateau ice thickness (4Ob5) has a surface change of 29.2°. This illustrates how a retreating ice sheet settles  
180 into the terrain following flow that results in fjord formation. As with parallel simulations, the thickness of the temperate ice layer is consistently much lower than for perpendicular simulations (Fig. 6c).

### 3.4 Smoothed control simulation

The perpendicular simulation with 1,000 m plateau ice thickness and 850 m a<sup>-1</sup> target surface velocity (8Pe10) has an area-averaged driving stress of 424.8 kPa when real topography is used. In comparison, the smoothed topography simulation  
185 (8Sm10) with equivalent parameters has an area-averaged driving stress of only 295.2 kPa. In this case using a smooth or low fidelity subglacial topography underestimates the driving stress required for equivalent average surface velocity by 43.9%. This effect increases as plateau ice thickness decreases. Comparing the corresponding simulations at 500 m a<sup>-1</sup> (8Pe5 and 8Sm5) gives a difference of 227.2 kPa or 88.9%. On average for all perpendicular simulations, this discrepancy is larger than comparing perpendicular flow to parallel flow at Veafjorden (Table 2).

190 After decreasing the slope by 0.40°, the smoothed topography simulation (8Sm10) has a similar surface flow field to the real topography simulation (8Pe10) (Fig. 7d,h). When comparing local surface velocity over the fjord, both slow down by roughly the same amount. The smoothed control is reduced to 778.1 m a<sup>-1</sup> while the real topography simulation is reduced to 782.3 m a<sup>-1</sup>. Both reach roughly 920 m a<sup>-1</sup> at maximum. Nonetheless, the enthalpy fields, and hence rheological characteristics,

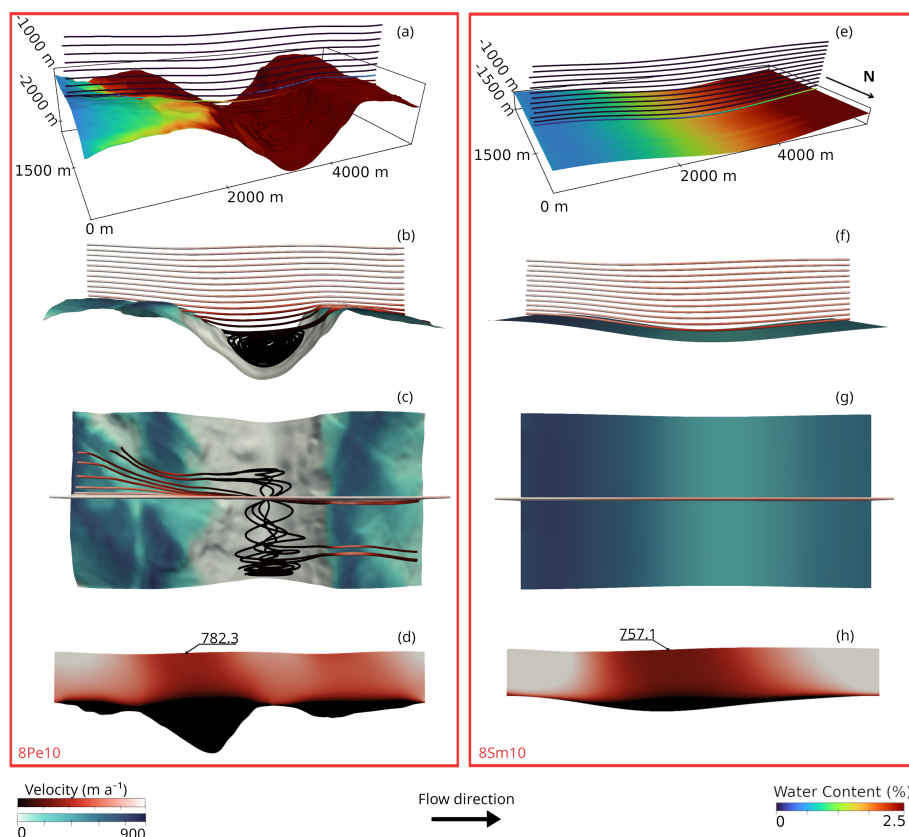


**Figure 7.** A comparison of Veafjorden perpendicular, 1,000 m plateau ice thickness,  $850 \text{ m a}^{-1}$  simulation to perpendicular smoothed control. Perpendicular Veafjorden 8Pe10 (a–d). Perpendicular (Smoothed Control) 8Sm10 (e–h). Note that panel (d) and (h) includes tapering region.

195 between the two settings differ substantially (Fig. 7) with the water content in the control not approaching that of the real topography simulation. Furthermore, there is no indication of flow reversal or Moffatt eddies.

#### 4 Discussion

200 Our results show that realistic fjord geometries — which are (i) common across the western margin of the palaeo-Scandinavian ice sheet, (ii) likely present beneath the margins of the present day GrIS, and (iii) largely excluded from large-scale ice-sheet models — significantly complicate patterns of ice motion and temperate ice. In contrast to smoothed topography, real topography can result in much higher driving stresses required to achieve the same surface velocity, with clear evidence for a strong anisotropic response of ice motion to the alignment of the underlying landscape. Features as dramatic as Moffatt eddies (Gudmundsson, 1997; Meyer and Creyts, 2017) may at first appear to be isolated features with limited influence on overall



ice-sheet motion: our results and analysis of flow-aligned slope angles in western Norway (Fig. 1) suggest that they are likely a ubiquitous feature of ice motion over incised fjord landscapes.

205 Deep fjords furthermore present an obstacle to suggestions that basal traction should be treated as bounded across all glacier and ice-sheet settings (e.g. Schoof, 2005; Minchew and Joughin, 2020; Zoet and Iverson, 2020; Helanow et al., 2021). In bounded basal traction relationships the traction provided by the bed approaches a maximum value that it does not exceed (such as the regularised-Coulomb relationship used as the base for this model, Eq. 11), while in unbounded basal traction relationships basal traction will continue increasing as basal velocity increases (such as Weertman sliding, Weertman (1957)).  
 210 For hard beds, the suggestion of bounded basal traction follows from Iken’s bound (Iken, 1981; Schoof, 2005), usually defined as

$$\frac{\tau_b}{N} \leq \tan(\beta) \quad (13)$$

where  $\tau_b$  is the basal traction,  $N = p_i - p_w$  is the effective pressure at the base where  $p_i$  and  $p_w$  are ice and water pressures respectively, and  $\beta$  is the maximum up-slope angle in the mean flow direction. However, Eq. 13 ceases to become an effective  
 215 bound in the situation of very steep surfaces, and furthermore omits traction provided at the ice-bed interface itself. In the case of ice flow oriented perpendicular to the near-vertical cliffs present on Veafjorden’s western side (Fig. 8), there is no theoretical bound to the resistive traction that could be provided by the cliffs to oppose ice motion. If the ice is effectively ‘locked in’ to the landscape as a result of rough topography, with very low, or even reversed basal slip (Fig. 5), then resistance to ice motion comes from the deformation of the ice itself which has a non-linear viscous rheology (Nye, 1953; Glen, 1955), or potentially  
 220 even linear for temperate ice (Schohn et al., 2025; Adams et al., 2021). Taking a vertical line through the centre-point of the fjord in isolation, where velocity at the fjord base is  $\sim 0.5\text{-}1 \text{ m a}^{-1}$  in the opposite direction to the surface orientation, resistance to driving stress,  $\tau_s$ , is then provided by viscous deformation within and below the shear band spanning the fjord hollow and can be expressed as

$$\tau_s = A \int_{z_b}^{z_s} (2\dot{\epsilon}_e)^{\frac{1}{n}} dz \quad (14)$$

225 where  $A$  and  $n$  refer to values in the Nye-Glen isotropic flow law (Eq. 4),  $\dot{\epsilon}_e^2 = \frac{1}{2} \text{tr}(\dot{\epsilon}^2)$ , and  $z_b$  and  $z_s$  refer to the positions of the fjord base and top of the shear band, respectively. If a large-scale ice sheet model takes a smoothed basal surface rather than the actually existing rough topography, or if the discretisation of the model domain simply does not allow for features such as fjords to be accurately resolved (Fig. 8), then shear-band features such as those we simulate here for perpendicular flow will be implicitly subsumed into the basal sliding relationship – even if it is not expressly formulated or suitable for handling  
 230 such deformation features. In the case of a deep fjord, it is simple to see how its entire span could be captured within a single  $\sim 2 \text{ km}$  numerical model grid cell. If these features are inadvertently incorporated within sliding parameterisations we should expect at least a component of resistance to ice motion to follow an unbounded power-law (Eq. 14), rather than ice-sheet sliding being bounded in all settings (Minchew and Joughin, 2020). Veafjorden is a dramatic example, but slopes, cliffs, and fjords



which exceeding  $30^\circ$  in the palaeo flow direction are common across western Norway (Fig. 1), providing many more possible  
 235 settings where resistance to ice motion is controlled by viscous ice deformation prompted by rough topography that would  
 not otherwise be captured in the basal boundary position used in large-scale ice sheet models. Furthermore, features such as  
 those modelled in this paper, even if sporadically placed, may still exert an important influence on regional ice-sheet motion  
 through lateral and longitudinal stresses. Further work is required to fully isolate these interactions and their scale dependence,  
 but such features may go some distance to providing a physically based background to the persistent utility of power-law  
 240 sliding relationships across the GrIS (Maier et al., 2021), which often invoke Weertman sliding (Weertman, 1957), even if the  
 underlying assumptions are not entirely realistic (Weertman, 1979).

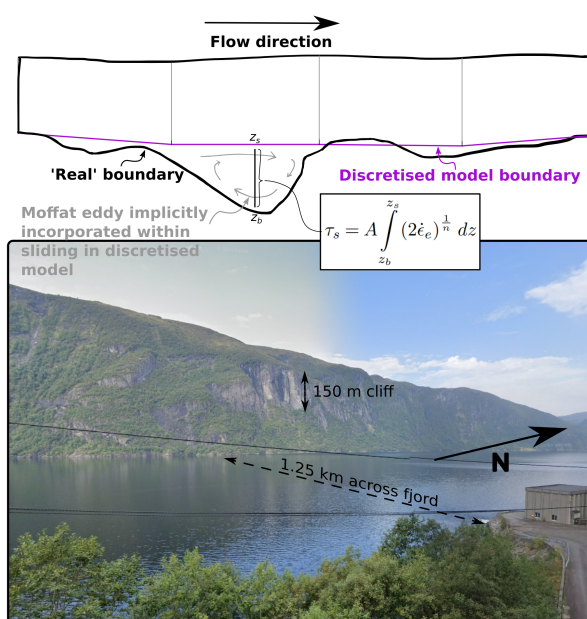


**Figure 8.** View of vertical cliffs on Veafjorden’s western side from the E16 road at 60.508903 N, 5.725418 E. Image: © Google, captured from Google Street View.

A possible barrier to this viewpoint is cavitation. In the two-dimensional settings of Schoof (2005) and Gagliardini et al. (2007) cavities gradually overwhelm geometric depressions as  $u_b$  increases, lowering  $\tau_b$ . These two studies non-dimensionalise the domain such that the sinusoidal beds they use may be taken as an approximation of small-scale roughness or fjord geometry.  
 245 However, Veafjorden features clear hydrological escape pathways both north and south (Figs. 1, 2). Combined with a palaeo ice sheet surface that would induce regional hydrological gradients towards the ocean, a very large cavity within Veafjorden in line with the models of Schoof (2005) and Gagliardini et al. (2007) seems unlikely. And, even in the perhaps implausible situation where a cavity occupies a space as large as the present day ocean within Veafjorden (Fig. 8), cliffs facing perpendicular to oncoming ice would still be present at the ice-bed interface. Regardless, determining the configuration of subglacial cavities in



250 a setting such as Veafjorden, rather than a region that is approximately flat at the macro scale, remains an important outstanding question for subglacial hydrology.

The landscape of western Norway does not represent a one-to-one mapping of the subglacial landscape of Earth's presently existing ice sheets, but there are many similarities, particularly for the GrIS. Areas of high relief (>1,000 m a.s.l.) with deep fjords are easily observable at both the western and eastern margins of the GrIS, with continuation of these fjords inland beneath the ice evident until BedMachine mapping begins to lose its sharpness (Morlighem et al., 2017). Flow-aware hill-shading of the GrIS surface (MacGregor et al., 2024) and analysis of radio-echo flight lines (Paxman et al., 2024) also highlights locations across the GrIS where ice flow is inferred to cross subglacial valleys perpendicularly. In multiple fast-flowing regions close to the margins of the GrIS, inferred subglacial topography features from MacGregor et al. (2024) appear to align with surface velocity variations in excess of  $100 \text{ m a}^{-1}$ , reflecting the surface velocity variations modelled in this study (Fig. A2). In Antarctica, the Aurora Subglacial Basin and Gamburtsev Mountains in particular exhibit subglacial valleys that cross cut the present-day prevailing flow direction, which likely originated during the initial inception of the AIS (Young et al., 2011; Meyer and Creyts, 2017). Basal traction inversions from both the GrIS and AIS furthermore evidence complex banded patterns (Sergienko et al., 2014). In Sergienko et al. (2014) these are hypothesised to result from pattern-forming instabilities in subglacial water pressure. We suggest that they may in fact reflect varying resistance as a result of subglacial topography. Notably, this implies that the patterns are potentially much longer lasting than would be the case if they were solely a result of subglacial hydrology variations, and places an emphasis on the role of basal topography patterns on basal traction at the intermediate scale, rather than solely variations in basal material properties at the micro scale.

Our results also point to anisotropic resistance provided by subglacial landscapes, which has been previously explored in an idealised case (Hindmarsh, 2000). Given we look at topography from beneath a palaeo ice sheet, fjord orientations vary widely (Fig. 1), and our results indicate that ice-motion orientation variations significantly influence the resistance from topography (Fig. 3), we can conclude that basal traction patterns should be expected to vary over the lifecycle of an ice sheet, as drainage basins evolve and ice motion patterns shift during growth and decay. We leave direct quantification of the influence of landscape anisotropy on basal sliding relationship anisotropy for future work, but also note that the impact of basal sliding anisotropy will be small for most predictive timescales (100-1,000 yr) in the event that flow orientations do not shift substantially.

## 275 5 Conclusions

We show that incised fjord landscapes induce significant complications into ice sheet motion, prompting a required increase in driving stress of up to ~41–89% when oriented perpendicular to flow compared to smoothed topography. Realistic fjord topographies will also introduce anisotropy into a landscape's basal traction response at a macro scale, and may furthermore invalidate the assumptions behind bounded traction at these scales. It is evidently presently infeasible and impractical to incorporate this behaviour into large-scale ice sheet models directly due to computational limitations on resolution, with bed topography products furthermore lacking the fidelity to resolve such features. Instead, future work should focus on parameterising the net influence of this behaviour — and that caused by other large-scale topographic obstacles — on basal traction

<https://doi.org/10.5194/egusphere-2025-1304>

Preprint. Discussion started: 28 April 2025

© Author(s) 2025. CC BY 4.0 License.



relationships at the more relevant macro scale, with particular reference to the viscous component of ice deformation that may unwittingly fall within the basal sliding relationship. Doing so may contribute to alleviating uncertainties in predictions of sea level rise (Aschwanden et al., 2021), and to reducing the share of uncertainty in basal traction inversions that pertains directly to sliding processes (Berends et al., 2023).

*Code and data availability.* Elmer/Ice solver input files, post-processing scripts, and ParaView visualisation files available at <https://doi.org/10.5281/zenodo.15052902> (Barndon, 2025)



### Appendix A: Calculating flow-aligned hill slope

290 To quantify the topographic gradient in the direction of surface flow, we computed the flow-aligned gradient using DEM data and flow velocity components. Partial derivatives of elevation in the x- and y-directions ( $\frac{dz}{dx}$  and  $\frac{dz}{dy}$ , hereafter  $p$  and  $q$ , respectively) were computed from the DEM by fitting a third-order polynomial to a 5x5 window following Florinsky (2017). Flow direction was determined from velocity components  $v_x$  and  $v_y$ , with velocity magnitude  $v_v = \sqrt{v_x^2 + v_y^2}$  used to compute unit vectors in the flow direction:

$$295 \quad \hat{v} = \left( \frac{v_x}{v_v}, \frac{v_y}{v_v} \right) \tag{A1}$$

The gradients  $p$  and  $q$  were then projected onto the flow direction by computing the dot product:

$$\text{Flow-Aligned Gradient} = p \cdot \frac{v_x}{v_v} + q \cdot \frac{v_y}{v_v} \tag{A2}$$

The resulting flow-aligned gradient represents the topographic slope in the direction of flow.

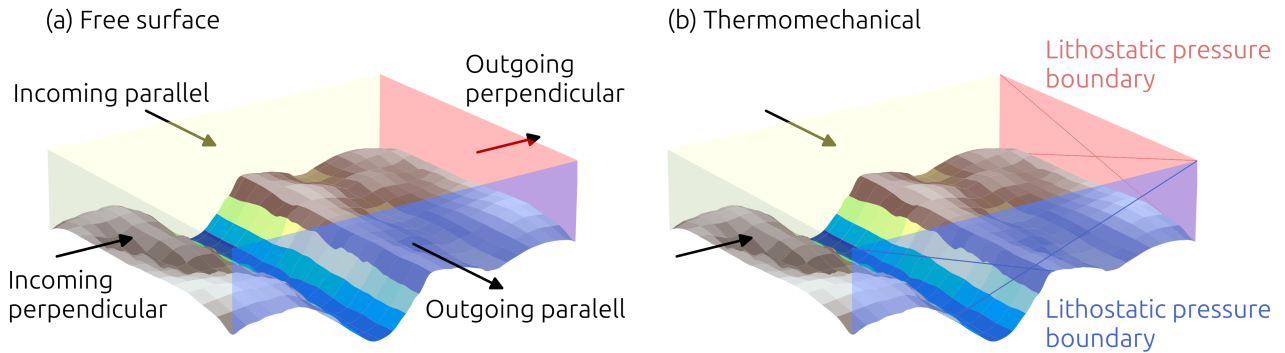


**Figure A1.** The incoming and outgoing boundaries for the two simulation steps (a) Free surface stage and (b) Thermomechanically coupled stage. Illustrated parallel flow direction and boundary does not represent simulated orientation.

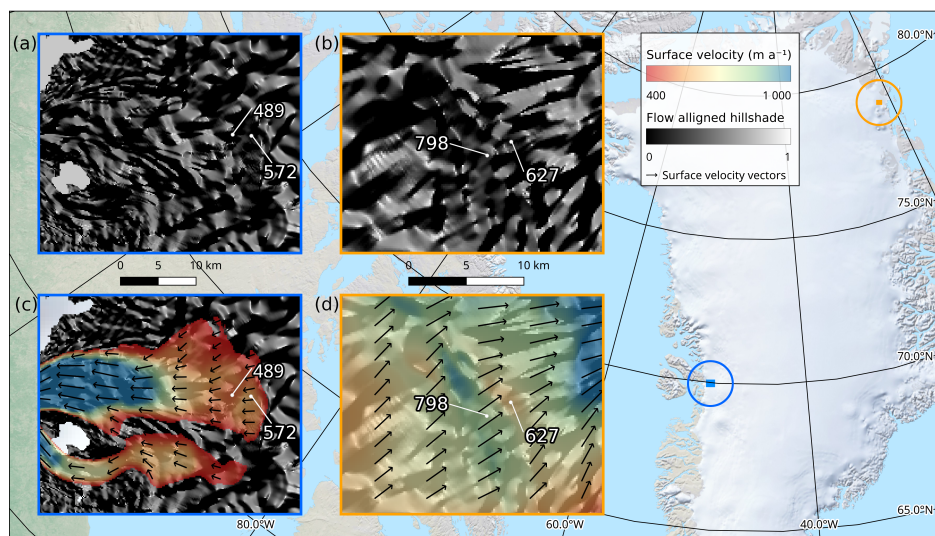


**Figure A2.** Two example locations in Greenland with variable surface velocity along the same flow line. **(a–b)** Hill-shade of basal topography with the azimuth computed along the direction of flow (MacGregor et al., 2015). The hill-shade indicate possible areas of subglacial obstacles or valleys. **(c–d)** Surface velocity data mapped on top of the flow aligned hill-shade in **(a)** and **(b)**. Several places in the two examples have velocity differences of more than  $100 \text{ m a}^{-1}$ . Black arrows represent flow direction vectors. Velocity data from Joughin et al. (2010); Joughin (2022); Moon et al. (2023).

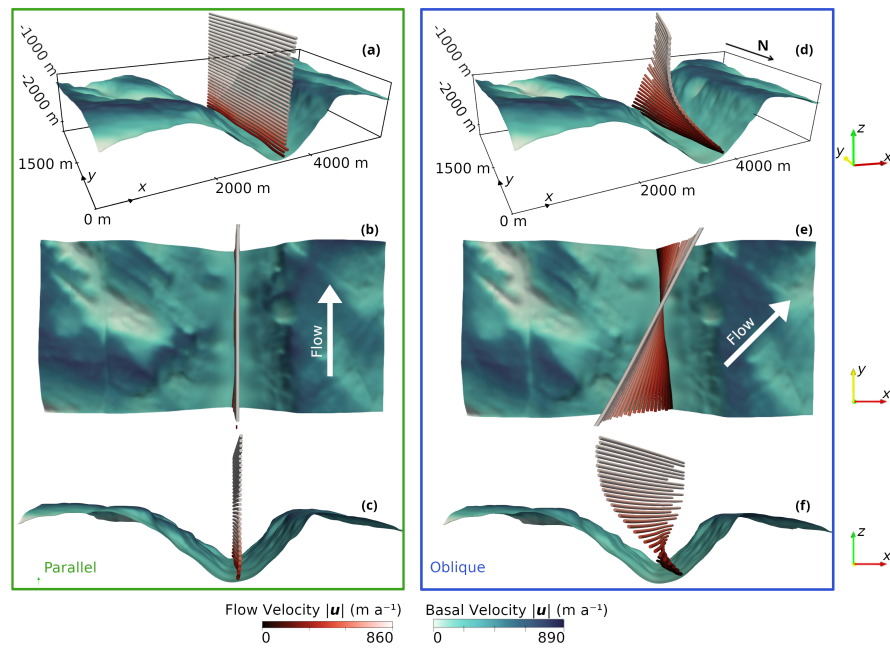


**Figure A3.** A comparison of parallel flow (a) to (c) from run 8Pa10, and oblique flow (d) to (f) from run 8Ob10. Both have a target velocity of  $850 \text{ m a}^{-1}$  and plateau ice thickness of 1000 m.



**Table A1.** Model parameters.

Symbol	Units	Variable	Value	Citation
$A_1$	MPa a <sup>-1</sup>	Rate factor 1	$9.133 \times 10^{12}$	
$A_2$	MPa a <sup>-1</sup>	Rate factor 2	$7.477 \times 10^{23}$	
$A_{max}$	MPa a <sup>-1</sup>	Limiting rate factor		
$A_s$	m a <sup>-1</sup> MPa <sup>-n</sup>	Sliding coefficient	$2.13 \times 10^4$	Average of Helanow et al. (2021) values
$C$		Maximum slope value	0.16167	Average of Helanow et al. (2021) values
$C_a$	J kg <sup>-1</sup> K <sup>-2</sup>	Enthalpy heat capacity A	7.253	Gilbert et al. (2014)
$C_b$	J kg <sup>-1</sup> K <sup>-1</sup>	Enthalpy heat capacity B	146.3	Gilbert et al. (2014)
$G_b$	W m <sup>-2</sup>	Geothermal heat flux	$55 \times 10^{-3}$	Cook et al. (2020)
$L$	J kg <sup>-1</sup>	Latent heat of fusion of ice	$3.34 \times 10^5$	
$\kappa_c$	kg m <sup>-1</sup> a <sup>-1</sup>	Cold ice enthalpy diffusivity	$1.024 \times 10^{-3}$	Gilbert et al. (2014)
$\kappa_t$	kg m <sup>-1</sup> a <sup>-1</sup>	Temperate ice enthalpy diffusivity	$1.045 \times 10^{-4}$	Gilbert et al. (2014)
$p_{tr}$	MPa	Triple-point pressure of water	0.612	
$Q_1$	J mol <sup>-1</sup>	Activation energy 1	$60 \times 10^3$	
$Q_2$	J mol <sup>-1</sup>	Activation energy 2	$115 \times 10^3$	
$\rho_i$	kg m <sup>-3</sup>	Ice density	910	
$T_{lim}$	K	Limit temperature	263.2	Cuffey and Paterson (2010)
$T_{ref}$	K	Reference temperature	200	
$T_{tr}$	K	Triple-point temperature of water	273.2	
$W_1$	MPa a <sup>-1</sup>	Water viscosity factor 1	1.0	Duval (1977)
$W_2$	MPa a <sup>-1</sup>	Water viscosity factor 2	2.35	
$W_3$	MPa a <sup>-1</sup>	Water viscosity factor 3	77.945	
$\omega_{lim}$	Proportion	Upper water limit	0.025	



300 *Author contributions.* S Barndon ran the simulations and wrote the first version of the manuscript with support from RL and AB. TC produced scripts for Fig. 1. S Brechtelsbauer handled the conversion of geospatial data required for Fig. 1. All authors contributed to the final version of the manuscript.

*Competing interests.* The contact author has declared that none of the authors has any competing interests.

*Acknowledgements.* We thank Jan Mangerud for early discussions on flow orientations in western Norway.



## References

- 305 Adams, C. J. C., Iverson, N. R., Helanow, C., Zoet, L. K., and Bate, C. E.: Softening of Temperate Ice by Interstitial Water, *Frontiers in Earth Science*, 9, <https://doi.org/10.3389/feart.2021.702761>, 2021.
- Aschwanden, A., Bartholomaus, T. C., Brinkerhoff, D. J., and Truffer, M.: Brief communication: A roadmap towards credible projections of ice sheet contribution to sea level, *The Cryosphere*, 15, 5705–5715, <https://doi.org/10.5194/tc-15-5705-2021>, 2021.
- Barndon, S.: Supplementary data for "Ice motion across incised fjord landscapes", <https://doi.org/10.5281/zenodo.15052902>, 2025.
- 310 Berends, C. J., van de Wal, R. S. W., van den Akker, T., and Lipscomb, W. H.: Compensating errors in inversions for subglacial bed roughness: same steady state, different dynamic response, *The Cryosphere*, 17, 1585–1600, <https://doi.org/10.5194/tc-17-1585-2023>, 2023.
- Bernard, M., Steer, P., Gallagher, K., and Egholm, D. L.: The Impact of Lithology on Fjord Morphology, *Geophysical Research Letters*, 48, e2021GL093101, <https://doi.org/https://doi.org/10.1029/2021GL093101>, e2021GL093101 2021GL093101, 2021.
- Briner, J. P., Miller, G. H., Finkel, R., and Hess, D. P.: Glacial erosion at the fjord onset zone and implications for the organization of ice flow  
315 on Baffin Island, Arctic Canada, *Geomorphology*, 97, 126–134, <https://doi.org/https://doi.org/10.1016/j.geomorph.2007.02.039>, *glacial Landscape Evolution - Implications for Glacial Processes, Patterns and Reconstructions*, 2008.
- Castleman, B. A., Schlegel, N.-J., Caron, L., Larour, E., and Khazendar, A.: Derivation of bedrock topography measurement requirements for the reduction of uncertainty in ice-sheet model projections of Thwaites Glacier, *The Cryosphere*, 16, 761–778, <https://doi.org/10.5194/tc-16-761-2022>, 2022.
- 320 Christ, A. J., Rittenour, T. M., Bierman, P. R., Keisling, B. A., Knutz, P. C., Thomsen, T. B., Keulen, N., Fosdick, J. C., Hemming, S. R., Tison, J.-L., Blard, P.-H., Steffensen, J. P., Caffee, M. W., Corbett, L. B., Dahl-Jensen, D., Dethier, D. P., Hidy, A. J., Perdrial, N., Peteet, D. M., Steig, E. J., and Thomas, E. K.: Deglaciation of northwestern Greenland during Marine Isotope Stage 11, *Science*, 381, 330–335, <https://doi.org/10.1126/science.ade4248>, 2023.
- Cook, S. J., Christoffersen, P., Todd, J., Slater, D., and Chauché, N.: Coupled modelling of subglacial hydrology and calving-front melting  
325 at Store Glacier, West Greenland, *The Cryosphere*, 14, 905–924, <https://doi.org/10.5194/tc-14-905-2020>, 2020.
- Copernicus DEM: Copernicus DEM - Global and European Digital Elevation Model, <https://dataspace.copernicus.eu/explore-data/data-collections/copernicus-contributing-missions/collections-description/COP-DEM>, <https://doi.org/https://doi.org/10.5270/ESA-c5d3d65>, [Accessed 18-03-2025], 2024.
- Cuffey, K. M. and Paterson, W. S. B.: *The Physics of Glaciers*, Butterworth-Heinemann, Academic Press, 2010.
- 330 Duval, P.: The Role Of The Water Content On The Creep Rate Of Polycrystalline Ice., *Int. Assoc. Hydrol. Sci. Publ.*, 118, 29–33, 1977.
- Florinsky, I. V.: An illustrated introduction to general geomorphometry, *Progress in Physical Geography*, 41, 723–752, <https://doi.org/10.1177/0309133317733667>, 2017.
- Frank, T., Åkesson, H., de Fleurian, B., Morlighem, M., and Nisancioglu, K. H.: Geometric controls of tidewater glacier dynamics, *The Cryosphere*, 16, 581–601, <https://doi.org/10.5194/tc-16-581-2022>, 2022.
- 335 Gagliardini, O., Cohen, D., Råback, P., and Zwinger, T.: Finite-element modeling of subglacial cavities and related friction law, *Journal of Geophysical Research: Earth Surface*, 112, <https://doi.org/https://doi.org/10.1029/2006JF000576>, 2007.
- Gagliardini, O., Zwinger, T., Gillet-Chaulet, F., Durand, G., Favier, L., de Fleurian, B., Greve, R., Malinen, M., Martín, C., Råback, P., Ruokolainen, J., Sacchetti, M., Schäfer, M., Seddik, H., and Thies, J.: Capabilities and performance of Elmer/Ice, a new-generation ice sheet model, *Geoscientific Model Development*, 6, 1299–1318, <https://doi.org/10.5194/gmd-6-1299-2013>, 2013.



- 340 Gee, D. G., Fossen, H., Henriksen, N., and Higgins, A. K.: From the Early Paleozoic Platforms of Baltica and Laurentia to the Caledonide Orogen of Scandinavia and Greenland, *International Union of Geological Sciences*, 31, 44–51, <http://episodes.org/journal/view.html?doi=10.18814/epiiugs/2008/v31i1/007>, 2008.
- Gilbert, A., Gagliardini, O., Vincent, C., and Wagon, P.: A 3-D thermal regime model suitable for cold accumulation zones of polythermal mountain glaciers, *Journal of Geophysical Research: Earth Surface*, 119, 1876–1893, <https://doi.org/https://doi.org/10.1002/2014JF003199>, 2014.
- 345 Glen, J. W.: The Creep of Polycrystalline Ice, *Proceedings of the Royal Society of London. Series A, Mathematical and Physical Sciences*, 228, 519–538, <http://www.jstor.org/stable/99642>, 1955.
- Gudmundsson, G. H.: Basal-flow characteristics of a non-linear flow sliding frictionless over strongly undulating bedrock, *Journal of Glaciology*, 43, 80–89, <https://doi.org/10.3189/S0022143000002835>, 1997.
- 350 Harbor, J. M.: Numerical modeling of the development of U-shaped valleys by glacial erosion, *GSA Bulletin*, 104, 1364–1375, [https://doi.org/10.1130/0016-7606\(1992\)104<1364:NMOTDO>2.3.CO;2](https://doi.org/10.1130/0016-7606(1992)104<1364:NMOTDO>2.3.CO;2), 1992.
- Harbor, J. M., Hallet, B., and Raymond, C. F.: A numerical model of landform development by glacial erosion, *Nature*, 333, 347–349, <https://doi.org/10.1038/333347a0>, 1988.
- Haseloff, M., Hewitt, I. J., and Katz, R. F.: Englacial Pore Water Localizes Shear in Temperate Ice Stream Margins, *Journal of Geophysical Research: Earth Surface*, 124, 2521–2541, <https://doi.org/https://doi.org/10.1029/2019JF005399>, 2019.
- 355 Helanow, C., Iverson, N. R., Woodard, J. B., and Zoet, L. K.: A slip law for hard-bedded glaciers derived from observed bed topography, *Science Advances*, 7, eabe7798, <https://doi.org/10.1126/sciadv.abe7798>, 2021.
- Hindmarsh, R. C.: Sliding over anisotropic beds, *Annals of Glaciology*, 30, 137–145, <https://doi.org/10.3189/172756400781820840>, 2000.
- Iken, A.: The Effect of the Subglacial Water Pressure on the Sliding Velocity of a Glacier in an Idealized Numerical Model, *Journal of Glaciology*, 27, 407–421, <https://doi.org/10.3189/S0022143000011448>, 1981.
- 360 Joughin, I.: MEaSURES Greenland Annual Ice Sheet Velocity Mosaics from SAR and Landsat, Version 4, <https://doi.org/10.5067/RS8GFZ848ZU9>, 2022.
- Joughin, I., Smith, B. E., Howat, I. M., Scambos, T., and Moon, T.: Greenland flow variability from ice-sheet-wide velocity mapping, *Journal of Glaciology*, 56, 415–430, <https://doi.org/10.3189/002214310792447734>, 2010.
- 365 Jungdal-Olesen, G., Andersen, J. L., Born, A., and Pedersen, V. K.: The influence of glacial landscape evolution on Scandinavian ice-sheet dynamics and dimensions, *The Cryosphere*, 18, 1517–1532, <https://doi.org/10.5194/tc-18-1517-2024>, 2024.
- Kartverket: Depth data from the Norwegian Mapping Authority (Kartverket), <https://kartkatalog.geonorge.no/metadata/kartverket/dybdedata-terrengmodeller-dtm-wcs/8896c751-f3e0-4e4c-86e2-7579cea1f111>, 2024a.
- Kartverket: Elevation data from the Norwegian Mapping Authority (Kartverket), <https://hoydedata.no/LaserInnsyn2/>, 2024b.
- 370 Kleman, J., Hättestrand, C., Borgström, I., and Stroeven, A.: Fennoscandian palaeoglaciology reconstructed using a glacial geological inversion model, *Journal of Glaciology*, 43, 283–299, <https://doi.org/10.3189/S0022143000003233>, 1997.
- Kyrke-Smith, T. M., Gudmundsson, G. H., and Farrell, P. E.: Relevance of Detail in Basal Topography for Basal Slipperiness Inversions: A Case Study on Pine Island Glacier, Antarctica, *Frontiers in Earth Science*, 6, <https://doi.org/10.3389/feart.2018.00033>, 2018.
- Law, R., Christoffersen, P., MacKie, E., Cook, S., Haseloff, M., and Gagliardini, O.: Complex motion of Greenland Ice Sheet outlet glaciers with basal temperate ice, *Science Advances*, 9, eabq5180, <https://doi.org/10.1126/sciadv.abq5180>, 2023.
- 375 Løkkegaard, A., Mankoff, K. D., Zdanowicz, C., Clow, G. D., Lüthi, M. P., Doyle, S. H., Thomsen, H. H., Fisher, D., Harper, J., Aschwanden, A., Vinther, B. M., Dahl-Jensen, D., Zekollari, H., Meierbachtol, T., McDowell, I., Humphrey, N., Solgaard, A., Karlsson, N. B., Khan,



- S. A., Hills, B., Law, R., Hubbard, B., Christoffersen, P., Jacquemart, M., Seguinot, J., Fausto, R. S., and Colgan, W. T.: Greenland and Canadian Arctic ice temperature profiles database, *The Cryosphere*, 17, 3829–3845, <https://doi.org/10.5194/tc-17-3829-2023>, 2023.
- 380 MacGregor, J. A., Fahnestock, M. A., Catania, G. A., Paden, J. D., Prasad Gogineni, S., Young, S. K., Rybarski, S. C., Mabrey, A. N., Wagman, B. M., and Morlighem, M.: Radiostratigraphy and age structure of the Greenland Ice Sheet, *Journal of Geophysical Research: Earth Surface*, 120, 212–241, <https://doi.org/https://doi.org/10.1002/2014JF003215>, 2015.
- MacGregor, J. A., Colgan, W. T., Paxman, G. J. G., Tinto, K. J., Csathó, B., Darbyshire, F. A., Fahnestock, M. A., Kokfelt, T. F., MacKie, E. J., Morlighem, M., and Sergienko, O. V.: Geologic Provinces Beneath the Greenland Ice Sheet Constrained by Geophysical Data Synthesis, *Geophysical Research Letters*, 51, e2023GL107357, <https://doi.org/https://doi.org/10.1029/2023GL107357>, e2023GL107357 2023GL107357, 2024.
- 385 Maier, N., Gimbert, F., Gillet-Chaulet, F., and Gilbert, A.: Basal traction mainly dictated by hard-bed physics over grounded regions of Greenland, *The Cryosphere*, 15, 1435–1451, <https://doi.org/10.5194/tc-15-1435-2021>, 2021.
- Mangerud, J., Hughes, A. L., Sæle, T. H., and Svendsen, J. I.: Ice-flow patterns and precise timing of ice sheet retreat across a dissected fjord landscape in western Norway, *Quaternary Science Reviews*, 214, 139–163, <https://doi.org/https://doi.org/10.1016/j.quascirev.2019.04.032>, 2019.
- 390 Meyer, C. R. and Creyts, T. T.: Formation of ice eddies in subglacial mountain valleys, *Journal of Geophysical Research: Earth Surface*, 122, 1574–1588, <https://doi.org/https://doi.org/10.1002/2017JF004329>, 2017.
- Minchew, B. and Joughin, I.: Toward a universal glacier slip law, *Science*, 368, 29–30, <https://doi.org/10.1126/science.abb3566>, 2020.
- 395 Moffatt, H.: Viscous eddies near a sharp corner (Viscous eddy behavior near sharp corner, considering outer boundary conditions and stream function), *Archiwum Mechaniki Stosowanej*, 16, 365–372, 1964a.
- Moffatt, H. K.: Viscous and resistive eddies near a sharp corner, *Journal of Fluid Mechanics*, 18, 1–18, <https://doi.org/10.1017/S0022112064000015>, 1964b.
- Moon, T. A., Fisher, M., Stafford, T., and Thurber, A.: QGreenland (v3) [dataset], National Snow and Ice Data Center., <https://qgreenland.org>, 2023.
- 400 Morlighem, M., Williams, C. N., Rignot, E., An, L., Arndt, J. E., Bamber, J. L., Catania, G., Chauché, N., Dowdeswell, J. A., Dorschel, B., Fenty, I., Hogan, K., Howat, I., Hubbard, A., Jakobsson, M., Jordan, T. M., Kjeldsen, K. K., Millan, R., Mayer, L., Mouginot, J., Noël, B. P. Y., O’Cofaigh, C., Palmer, S., Rysgaard, S., Seroussi, H., Siegert, M. J., Slabon, P., Straneo, F., van den Broeke, M. R., Weinrebe, W., Wood, M., and Zinglensen, K. B.: BedMachine v3: Complete Bed Topography and Ocean Bathymetry Mapping of Greenland From Multibeam Echo Sounding Combined With Mass Conservation, *Geophysical Research Letters*, 44, 11,051–11,061, <https://doi.org/https://doi.org/10.1002/2017GL074954>, 2017.
- 405 Nye, J. F.: The Flow Law of Ice from Measurements in Glacier Tunnels, Laboratory Experiments and the Jungfraufirn Borehole Experiment, *Proceedings of the Royal Society of London. Series A, Mathematical and Physical Sciences*, 219, 477–489, <http://www.jstor.org/stable/99248>, 1953.
- 410 Ottesen, D., Dowdeswell, J. A., and Rise, L.: Submarine landforms and the reconstruction of fast-flowing ice streams within a large Quaternary ice sheet: The 2500-km-long Norwegian-Svalbard margin (57° - 80°N), *Geological Society of America Bulletin*, 117, 1033–1050, <https://doi.org/https://doi.org/10.1130/B25577.1>, 2005.
- Paxman, G. J.: Patterns of valley incision beneath the Greenland Ice Sheet revealed using automated mapping and classification, *Geomorphology*, 436, 108 778, <https://doi.org/https://doi.org/10.1016/j.geomorph.2023.108778>, 2023.



- 415 Paxman, G. J. G., Jamieson, S. S. R., Dolan, A. M., and Bentley, M. J.: Subglacial valleys preserved in the highlands of south and east Greenland record restricted ice extent during past warmer climates, *The Cryosphere*, 18, 1467–1493, <https://doi.org/10.5194/tc-18-1467-2024>, 2024.
- Reilly, E.: Ice Flow as an Indicator of Ice Thickness, Master of science thesis in quaternary geology, University of Bergen, 2023.
- Roldán-Blasco, J.-P., Gilbert, A., Piard, L., Gimbert, F., Vincent, C., Gagliardini, O., Togaibekov, A., Walpersdorf, A., and Maier, N.: Creep  
420 enhancement and sliding in a temperate, hard-bedded alpine glacier, *The Cryosphere*, 19, 267–282, <https://doi.org/10.5194/tc-19-267-2025>, 2025.
- Schohn, C. M., Iverson, N. R., Zoet, L. K., Fowler, J. R., and Morgan-Witts, N.: Linear-viscous flow of temperate ice, *Science*, 387, 182–185, <https://doi.org/10.1126/science.adp7708>, 2025.
- Schoof, C.: The effect of cavitation on glacier sliding, *Proceedings of the Royal Society A: Mathematical, Physical and Engineering Sciences*,  
425 461, 609–627, <https://doi.org/10.1098/rspa.2004.1350>, 2005.
- Sergienko, O. V., Creyts, T. T., and Hindmarsh, R. C. A.: Similarity of organized patterns in driving and basal stresses of Antarctic and Greenland ice sheets beneath extensive areas of basal sliding, *Geophysical Research Letters*, 41, 3925–3932, <https://doi.org/https://doi.org/10.1002/2014GL059976>, 2014.
- Svendsen, J. I. and Mangerud, J.: Late Weichselian and holocene sea-level history for a cross-section of western Norway, *Journal of Quaternary Science*, 2, 113–132, <https://doi.org/https://doi.org/10.1002/jqs.3390020205>, 1987.
- Weertman, J.: On the Sliding of Glaciers, *Journal of Glaciology*, 3, 33–38, <https://doi.org/10.3189/S0022143000024709>, 1957.
- Weertman, J.: The Unsolved General Glacier Sliding Problem, *Journal of Glaciology*, 23, 97–115, <https://doi.org/10.3189/S0022143000029762>, 1979.
- Wernecke, A., Edwards, T. L., Holden, P. B., Edwards, N. R., and Cornford, S. L.: Quantifying the Impact of Bedrock Topography Uncertainty in Pine Island Glacier Projections for This Century, *Geophysical Research Letters*, 49, e2021GL096589, <https://doi.org/https://doi.org/10.1029/2021GL096589>, e2021GL096589 2021GL096589, 2022.
- 435 Young, D. A., Wright, A. P., Roberts, J. L., Warner, R. C., Young, N. W., Greenbaum, J. S., Schroeder, D. M., Holt, J. W., Sugden, D. E., Blankenship, D. D., van Ommen, T. D., and Siegert, M. J.: A dynamic early East Antarctic Ice Sheet suggested by ice-covered fjord landscapes, *Nature*, 474, 72–75, <https://doi.org/10.1038/nature10114>, 2011.
- 440 Zoet, L. K. and Iverson, N. R.: A slip law for glaciers on deformable beds, *Science*, 368, 76–78, <https://doi.org/10.1126/science.aaz1183>, 2020.